

*1.7. NUCLEAR FIELD THEORY FOR PEDESTRIANS*

65

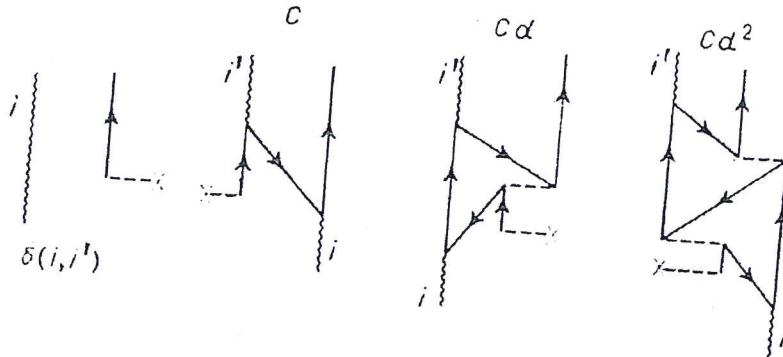


Figure 1.7.8: Lower order contributions to the one-particle transfer reaction induced by  $a_{m,1}^\dagger$ . The result of iterating the different contributions to all orders in  $1/\Omega$  is equal to  $T_{qm}(ii') = C \sum_n d^n = -\Lambda_i \Lambda_{i'} / (\omega_i - \epsilon_m)(E_{qm} - \epsilon_m - V)$ ,  $C = -\Lambda_i \Lambda_{i'} / (\omega_i - \epsilon_m)(E_{qm} - \epsilon_m)$ ,  $d = |V/(E_{qm} - \epsilon_m)|$ .

the amplitudes to  $(n = 1; m, 1)$  each weighted by the amplitude  $\xi_{iqm}$  given by eq. (1.7.61).

The lower-order contributions to the one-particle transfer amplitude between the state  $|n_i = 1\rangle$  and the state  $|qm\rangle$  are displayed in Fig. 1.7.8. They can be summed up to all orders of  $1/\Omega$ , the result being equal to

$$\begin{aligned}
 & \langle qm | a_{m,1}^\dagger | n_i = 1 \rangle \\
 &= \sum_{i'} \xi_{i'qm} \left\{ \delta(i, i') - \frac{\Lambda_i \Lambda_{i'}}{(\omega_i - \epsilon_m)(E_{qm} - \epsilon_m)} \left[ \frac{1}{1 - V/(E_{qm} - \epsilon_m)} \right] \right\} \\
 &= \sum_{i'} \xi_{i'qm} \{ \delta(i, i') - T_{qm}(i, i') \} \\
 &= -N_{qm} \left[ \frac{\Lambda_i}{\omega_i - E_{qm}} - \frac{\Lambda_i}{(\omega_i - \epsilon_m)(E_{qm} - \epsilon_m - V)} \sum_{i'} \frac{\Lambda_{i'}^2}{\omega_{i'} - E_{qm}} \right] \\
 &= \frac{N_{qm}(E_{qm} - \epsilon_m)\Lambda_i}{(E_{qm} - \omega_i)(\omega_i - \epsilon_m)}. \tag{1.7.77}
 \end{aligned}$$

This quantity is zero for the spurious roots (*i.e.*  $E_{qm} = \epsilon_m$ ) and agrees with the exact result for the  $\Omega - 1$  remaining physical roots.

Utilizing the relations

$$\frac{1}{V} = \sum_m \frac{1}{\epsilon_m - \omega_i}, \tag{1.7.78}$$

and

$$\frac{1}{V} = \sum_{m \neq m'} \frac{1}{\epsilon_{m'} - E_{qm}}, \tag{1.7.79}$$

and

$$|n0\lambda, j; IM\rangle = [\beta_n^\dagger(0\lambda)a_j^\dagger]_{IM}|0\rangle. \quad (1.7.86)$$

This constitutes the basis set of states  $\{\alpha_i\}$ . All other states give rise to the complementary Hilbert space  $\{a_i\}$ .

The elementary modes of excitation interact through the particle-vibration and four-point vertices displayed in Fig. 1.7.9 giving rise to the matrix elements

$$M_1(nj, n'j') \equiv \langle [\beta_n^\dagger(0\lambda)a_{j'}^\dagger]_{IM} | h_{eff}(E) | [\beta_n^\dagger(0\lambda)a_j^\dagger]_{IM} \rangle, \quad (1.7.87)$$

$$M_2(nj, n'j') \equiv \langle [\beta_{n'}^\dagger(2\lambda)a_{j'}^\dagger]_{IM} | h_{eff}(E) | [\beta_n^\dagger(2\lambda)a_j^\dagger]_{IM} \rangle, \quad (1.7.88)$$

and

$$M_3(nj, n'j') \equiv \langle [\beta_{n'}^\dagger(2\lambda)a_{j'}^\dagger]_{IM} | h_{eff}(E) | [\beta_n^\dagger(0\lambda)a_j^\dagger]_{IM} \rangle. \quad (1.7.89)$$

They are to be calculated by utilizing the graphical techniques of perturbation theory and the rules discussed in sect. 1.7.2. There are two parameters on which to expand upon in carrying out a perturbative calculation. The first one is the strength of the interaction vertices measured in terms of the average distance between single-particle levels. The second is  $1/\Omega$ , where  $\Omega = \sum_j(j + \frac{1}{2})$  is the effective degeneracy of the valence shells. These two parameters are in general connected through involved expressions. In the schematic model discussed in sect. 1.7.2, however, their relation is explicit and can be expressed as

$$\epsilon = O(1), \quad \Lambda = O\left(\frac{1}{\sqrt{\Omega}}\right) \quad \text{and} \quad V = O\left(\frac{1}{\Omega}\right). \quad (1.7.90)$$

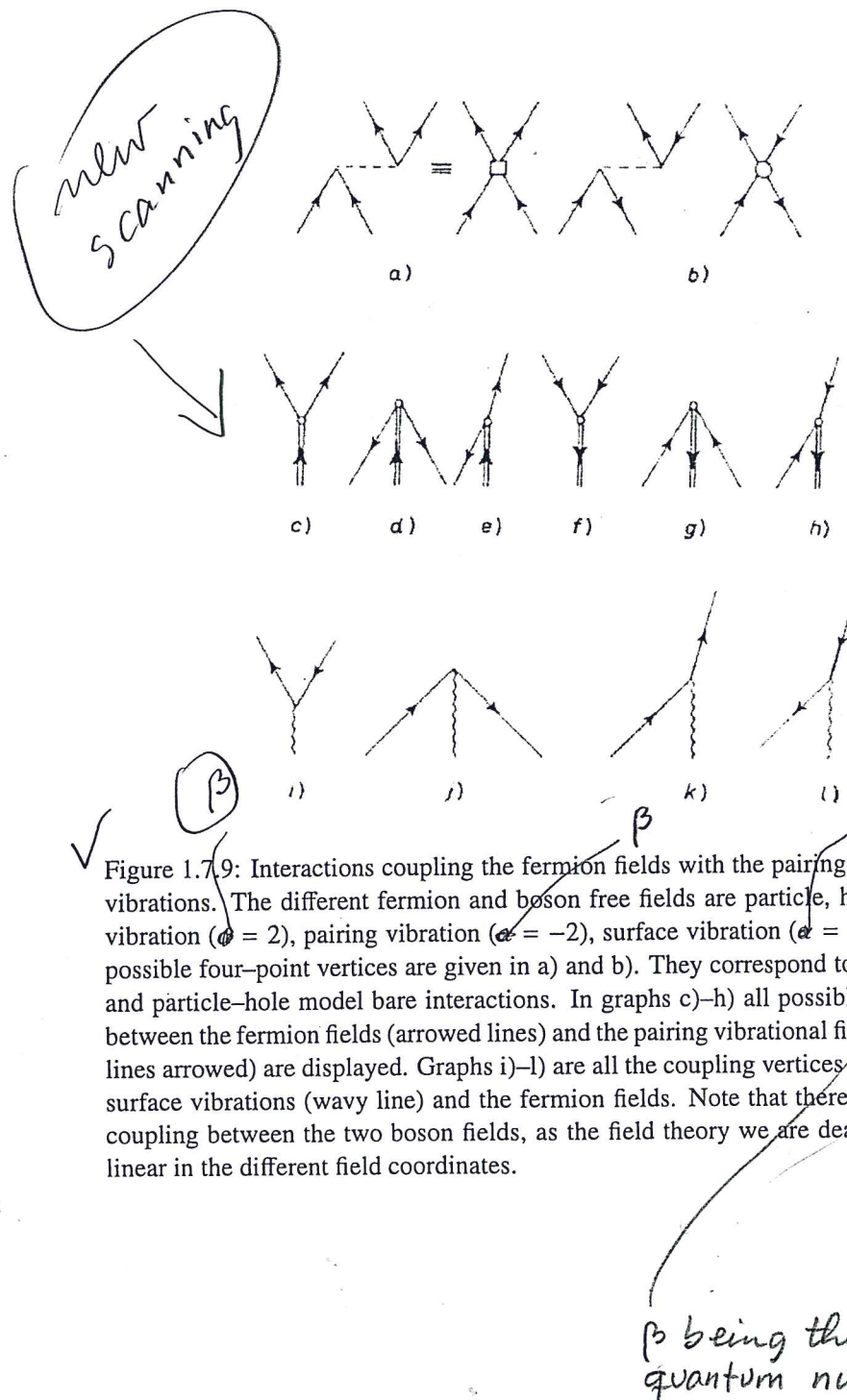
Another feature which determines the family of diagrams to select to a given order of perturbation is the number of internal lines which can be freely summed up. Each of these summations introduces a multiplicative factor  $\Omega$ . Because most of the present knowledge on the applicability of the field theoretical techniques rests upon schematic models, we utilize  $1/\Omega$  as the expansion parameter, and assume the relations (1.7.90) to be valid for more general situations. The nucleus  $^{209}\text{Bi}$  has been investigated by means of high-resolution anelastic process<sup>63</sup>. Through these experiments a septuplet of states around 2.6 MeV of excitation was identified, with spins ranging from  $\frac{3}{2}^+$  to  $\frac{15}{2}^+$ .

In zeroth order these states can be interpreted in terms of a proton moving in the  $h_{9/2}$  orbital coupled to the lowest octupole vibration of  $^{208}\text{Pb}$ . The  $\frac{3}{2}^+$  of this multiplet displays also a large parentage based on the proton pair addition and proton hole moving in the  $d_{3/2}$  orbital, as revealed by the  $(t, \alpha)$  reaction on  $^{210}\text{Po}$ <sup>64</sup>.

<sup>63</sup>Ungrin et al. (1971), Broglia, R. A. et al. (1970).

<sup>64</sup>Barnes, P. et al. (1972).

(in connection to this  
"standard" definition of  
we refer  
to footnote 55,  
p. 52)



✓ Figure 1.7.9: Interactions coupling the fermion fields with the pairing and surface vibrations. The different fermion and boson free fields are particle, hole, pairing vibration ( $\phi = 2$ ), pairing vibration ( $\phi = -2$ ), surface vibration ( $\epsilon = 0$ ). The two possible four-point vertices are given in a) and b). They correspond to the pairing and particle-hole model bare interactions. In graphs c)–h) all possible couplings between the fermion fields (arrowed lines) and the pairing vibrational fields (double lines arrowed) are displayed. Graphs i)–l) are all the coupling vertices between the surface vibrations (wavy line) and the fermion fields. Note that there is no direct coupling between the two boson fields, as the field theory we are dealing with is linear in the different field coordinates.

$\beta$  being the transfer quantum number.

$\beta = 2, \lambda$

### 1.7. NUCLEAR FIELD THEORY FOR PEDESTRIANS

69

The above results indicate that the (two-particle, one-hole) type of states in  $^{209}\text{Bi}$  are amenable to a simple description in term of the basis states

$$|2\lambda, j_1^{-1}; IM\rangle \equiv |j_1^{-1} \otimes \lambda^\pi(^{210}\text{Po}); IM\rangle \quad (\lambda^\pi = 0^+, 2^+, 4^+) \quad (1.7.91)$$

and

$\beta = 0, \lambda$

$$|0\lambda, j_2; IM\rangle \equiv |j_2 \otimes \lambda^\pi(^{208}\text{Pb}); IM\rangle \quad (\lambda^\pi = 3^-) \quad (1.7.92)$$

Only the lowest states of each spin and parity  $\lambda^\pi$  are included in the basis states, while all the RPA solutions are included in the intermediate states. The quadrupole surface vibration modes were allowed only as intermediate states. The single hole and particle states  $j_1^{-1}$  and  $j_2$ , respectively, correspond to experimentally known levels around the  $Z = 82$  shell closure. In what follows we discuss the different properties of the states generated by the basis spanned by the eigenvectors  $|2\lambda, j_1^{-1}; IM\rangle$  and  $|0\lambda, j_2; IM\rangle$ . We have divided the discussion in two parts. In the first part the two  $\frac{3}{2}^+$  states built out of the  $|d_{3/2}^{-1} \otimes gs(^{210}\text{Po})\rangle$  and  $|h_{9/2} \otimes 3^-(^{208}\text{Pb})\rangle$  configurations are studied in this space. This two-state system provides a rich laboratory to study the interplay of surface and pairing modes. In the second part the properties of the entire multiplet and of those states strongly excited in either the  $(t, \alpha)$  or  $(d, d')$  reactions are studied, in the complete configuration space.

what follows,

~~Other~~  $\frac{3}{2}^+$  states (The two states)

$$\alpha \quad \beta \equiv |d_{3/2}^{-1} \otimes gs(^{210}\text{Po}); 3/2^+\rangle \quad (1.7.93)$$

and

2.5

$$\beta \quad \beta \equiv |h_{9/2} \otimes 3^-(^{208}\text{Pb}); 3/2^+\rangle \quad (1.7.94)$$

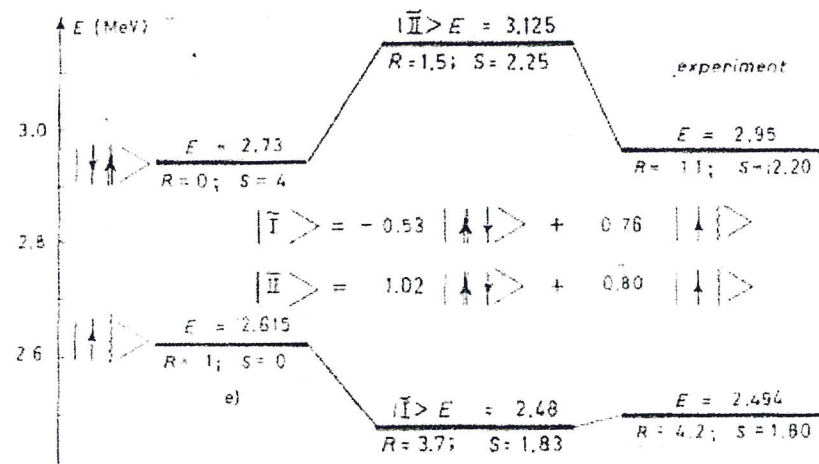
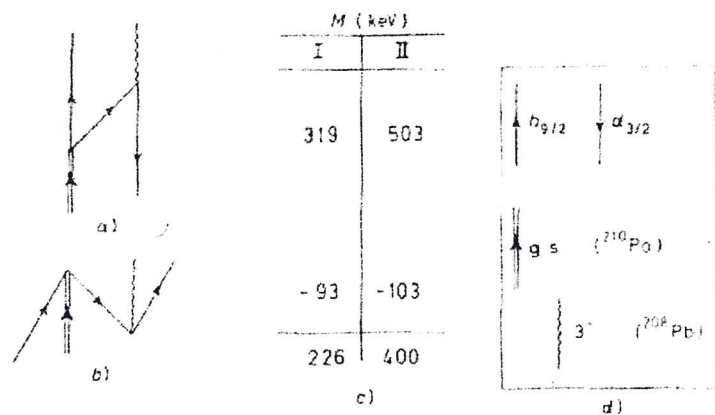
are 118 keV apart. They mix strongly through the couplings depicted by the graphs a) and b) of fig. 1.7.10. Because of the energy dependence of  $h_{eff}$  there is a different matrix element for each final state. The diagonalization of the matrices was carried out self-consistently, i.e. the energy denominators of the different graphs are to be calculated by utilizing the exact energies<sup>65</sup>. The corresponding graphical contributions to the spectroscopic factor and inelastic cross-sections are also collected in fig. 1.7.10. To be noted is the very different ratio of the  $(d, d')$  and  $(t, \alpha)$  cross sections. While  $R_1 = B(E3; (\frac{3}{2})_1)/B(E3; (\frac{3}{2})_2)$  is approximately equal to 1, the ratio  $R_2 = \sigma((t, \alpha); (\frac{3}{2})_2)/\sigma((t, \alpha); (\frac{3}{2})_1)$  is close to one. Because the component  $\beta$  carries the inelastic-scattering strength, while the  $(t, \alpha)$  reaction proceeds mainly through the component of type  $\beta$ , the difference between  $R_1$  and  $R_2$  can be traced back to the over-completeness of the basis which give rise to rather different normalizations of the two physical states. (see sect. 1.7.3, see also App. C)

<sup>65</sup>for more details, see ref. Bortignon, P. F. et al. (1977); see

Sect. 1.C.2)

also Bortignon et al (1976)

Stern



1.7. NUCLEAR FIELD THEORY FOR PEDESTRIANS

71

*Scam*

$$\left\{ \begin{array}{c} -0.53 \\ 1.02 \\ +0.103 \\ -0.103 \end{array} \right\} + \left\{ \begin{array}{c} 0.76 \\ 0.80 \\ -0.135 \\ 0.135 \end{array} \right\}^2 = 2 \times 10^{-2} \\ 1 \times 10^{-5}$$

$$4 \times \left\{ \begin{array}{c} -0.53 \\ 1.02 \\ +0.103 \\ -0.103 \end{array} \right\}^2 = 1.12 \\ 4.16$$

$$4 \times \left\{ \begin{array}{c} -0.53 \\ 1.02 \\ +0.103 \\ -0.103 \end{array} \right\} + \left\{ \begin{array}{c} 0.76 \\ 0.80 \\ -0.211 \\ 0.014 \\ -0.333 \\ 0.015 \end{array} \right\}^2 = 1.82 \\ 2.27$$

$$\frac{1}{10} \left\{ \begin{array}{c} 0.76 \\ 0.80 \\ -0.577 \end{array} \right\}^2 = 1.92 \times 10^{-2} \quad (3.3\%) \\ 2.13 \times 10^{-2} \quad (3.5\%)$$

better  
of coming

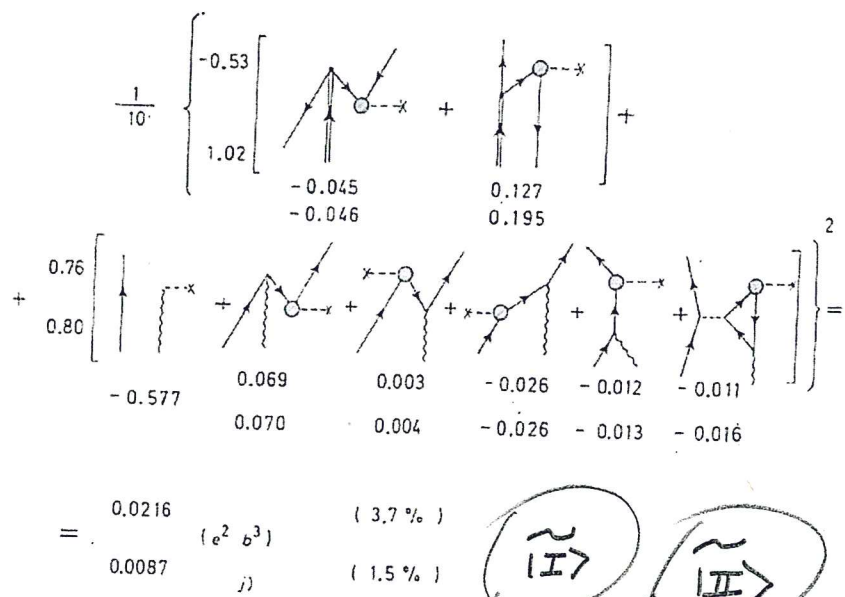


Figure 1.7.10: In a), b) and c) we give the two contributions to the matrix element  $M(E) = \langle d_{3/2}^{-1} \otimes gs(^{210}\text{Po}) | h_{eff}(E) | h_{9/2} \otimes 3^-(^{208}\text{Pb}); 3/2 \rangle$  in lowest order in  $1/\Omega$ . The resulting wave functions |I> and |II> are displayed in c) normalized according to (22). In e) we also give the unperturbed, theoretical energies of the levels. The  $(t, \alpha)$  spectroscopic factor corresponding to the reaction  $^{210}\text{Po}(t, \alpha)^{209}\text{Bi}$  is denoted by  $S$ , while

$$R = \frac{d\sigma(h_{9/2} \rightarrow J)}{d\sigma(qs(^{208}\text{Pb}) \rightarrow 3^-(^{208}\text{Pb}))}.$$

is the ratio of inelastic cross sections. In d) we display the free fields. The zeroth and order  $1/\Omega$  contributions to the electromagnetic excitations are collected in i) and j). The value  $0.58e^2b^3$  is the  $B(E3; 0 \rightarrow 3)$  value associated with the 2.615 MeV state in  $^{208}\text{Pb}$ . In g) and h) we give the zeroth and order  $1/\Omega$  contributions to the spectroscopic factor associated with the  $^{210}\text{Po}(t, \alpha)^{209}\text{Bi}$  reaction. Finally in f) we display the lowest contribution to the spectroscopic factor associated with the  $^{208}\text{Pb}({}^3\text{He}, d)$  reaction, which gives a measure of the ground state correlations of  $^{208}\text{Pb}$  associated with the existence of an octupole and a pairing vibration.

while in e) we provide a summary of the calculations in comparison with the data.

## 1.8 Competition between the variety of ZPF, in particular those associated with density ( $\beta = 0$ ) and pairing ( $\beta = \pm 2$ )

Particle-hole like vibrations, as e.g. collective surface quadrupole vibrations, induce dynamical distortions of the mean field which virtually break the magnetic degeneracy of levels into two-fold (Kramer's) degenerate (Nilsson-like) levels, thus effectively reducing the density of states (DOS) around the Fermi energy. In Fig. 1.8.1 is given a schematic representation of the subtle effects the interweaving of single-particle motion and collective vibrations has on pairing correlations, is attempted.

Pairing vibrations smooth out the sharp discontinuity of occupancy taking place at the Fermi energy displayed by closed shell systems, thus effectively concentrating into an effective, single  $j$ -shell, through dynamical  $(U_j V_j)$  weighting factors, the global degeneracy of levels in the energy region  $\epsilon_F \pm E_{corr}(\beta = \pm 2)$  (see Fig. 1.8.1 (g)).

Zero point fluctuations induced by particle-hole like and by pairing modes compete with each other for phase space, through Pauli principle (see Fig. 1.8.2), thus eventually leading to a single ground state containing all of the dressed renormalized ZPF (see Sect. 1.7). The Pauli principle NFT diagrams displayed in Figs. 1.8.2 (b) and 1.8.2 (d) are at the basis of the stabilization of the ground state in general and of the competition between (as a rule quadrupole) deformations in 3D space which breaks single-particle degeneracy (Nilsson potential), and in gauge space which thrives on large degeneracies<sup>66</sup>. It is also the reason why single open shell nuclei are usually spherical. When tidal-like polarization effects in doubly open shell nuclei become overwhelming, the nucleus makes use of a Jahn-Teller mechanism. This to profit at best and simultaneously, of the quadrupole-quadrupole (alignment) and of the pairing (independent pair motion in Kramers degenerate levels) interactions. In other words, of potential energy (quadrupole deformation, localization) and of pairs of nucleons solidly anchored to each other (localization), over distances  $\xi (\gg R_0)$  resulting in strongly overlapping entities and thus little sensitive to the orientation of the quadrupole deformed field (small moment of inertia), effect weakened in turn because of low spatial degeneracy. The fact that the moment of inertia  $\mathcal{J}$  of e.g. quadrupole deformed nuclei is found to be appreciably smaller (by about a factor of 2) than the rigid moment of inertia testifies to the role correlations play in nuclei. The fact that  $\mathcal{J}$  is considerably larger than the irrotational moment of inertia (by a factor of 5 cf. Bohr, A. and Mottelson (1975) p. 75) testifies to the subtle effects that spatial quantization, medium polarization effects, let alone the  $NN^{-1} S_0$  potential, eventually corrected by three-body effects, have in Cooper pair binding.

(within this context see Ch. 3, app. 3.13)

<sup>66</sup> Bayman (1961); Bès and Sorensen (1969); Mottelson (1962); Bohr, A. and Mottelson (1975).

This is an example of the competition between pairing and aligned scheme

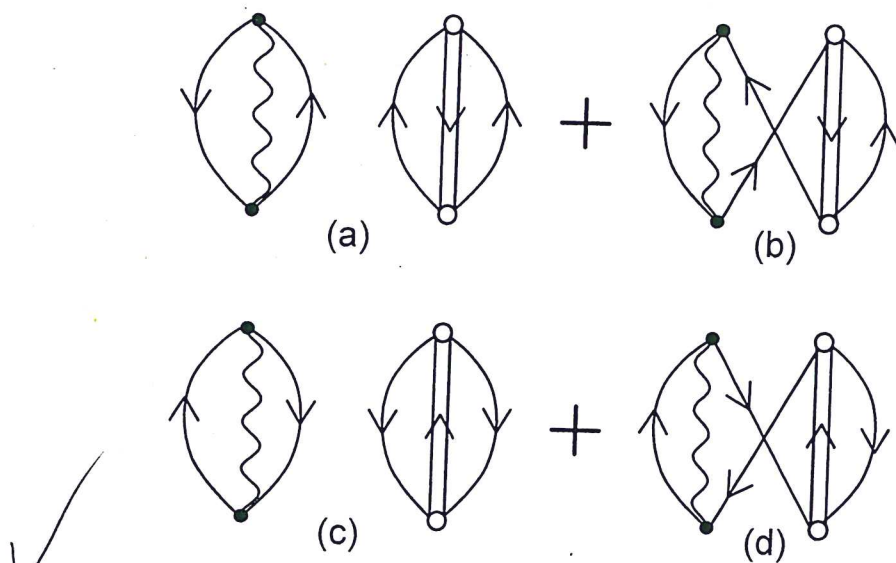


Figure 1.8.2: (a) (c) ZPF associated with  $p-h$  and pairing vibrations (pair subtraction and pair addition modes) make use of the same nucleon degrees of freedom to simultaneously, and independently, correlate  $p-h$ ,  $p-p$  and  $h-h$  excitations, thus violating Pauli principle (harmonic approximation). The NFT processes (b) and (d), which contribute to the correlation energy of the nucleus with opposite sign to that contributed by (a) and (c) (each unavoidable crossing of fermion lines contributes a minus sign), remove Pauli violating contributions to the corresponding order of perturbation.

in  $1/\Omega$

## 1.9 Optical potential and transfer

### 1.9.1 Bare particles and Hartree–Fock field

Nucleon elastic scattering experiments at energies of tens of MeV can be accurately described in terms of an optical potential in which the real component is parametrized according to the (Woods–Saxon) potential<sup>67</sup>,

$$U(r) = U f(r), \quad (1.9.1)$$

$f(r)$  being a Fermi (sigmoidal) function, of radius  $R_0 = r_0 A^{1/3}$  ( $r_0 = 1.27$  fm), diffusivity  $a = 0.57$  fm, and strength

$$U = U_0 + 0.4E \quad (1.9.2)$$

where

$$U_0 = \left( -51 + 33 \frac{N-Z}{A} \right) \text{ MeV}, \quad (1.9.3)$$

while  $E$  is the energy of the scattered particle  $\epsilon_k = \hbar^2 k^2 / 2m$ , measured from the Fermi energy. In the case of  ${}_{11}^{27}\text{Li}_8$ ,  $U_0 = 42$  MeV. One can replace the  $k$ -dependence in (1.9.2) by the so-called  $k$ -mass<sup>68</sup>

$$m_k = m \left( 1 + \frac{m}{\hbar^2 k} \frac{dU}{dk} \right)^{-1}, \quad (1.9.4)$$

where the energy independent Woods–Saxon potential has a depth given by  $(\frac{m}{m_k}) U_0 = U'_0$ .<sup>69</sup> For the nucleon of the core, i.e. of  ${}^9\text{Li}$ ,  $m_k = m(1+0.4)^{-1} \approx 0.7m$ . For the halo neutron<sup>70</sup>  $m_k = (1 + O \times 0.4)^{-1}$ , where  $O (= (R_0/R)^3)$  is the overlap between the core and the halo nucleons. From the  $R_0 = 2.69$  fm and  $R = 3.6$  fm one obtains  $m_k \approx 0.93 m$ .

<sup>67</sup>cf. e.g. Bohr and Mottelson (1969) and refs. therein.

<sup>68</sup>What in nuclear matter is called the  $k$ -mass and is a well defined quantity, in finite systems like the atomic nucleus, in which linear momentum is not a conserved quantity, is introduced to provide a measure of the non-locality of the mean field, and is defined for each state as the expectation value of the quantity inside the parenthesis in Eq. (1.9.4), calculated making use of the corresponding single-particle wavefunction (see e.g. ref. Bernard and Giai (1981), in which case  $m_k$  is referred to as the non-locality effective mass)

<sup>69</sup>See e.g. Fig. 2.14 Mahaux, C. et al. (1985).

<sup>70</sup>Assuming a velocity independent  $v$ , the dependence of the mean field stems from the exchange (Fock) potential  $U_x(\mathbf{r}, \mathbf{r}') = -\sum_i \varphi_i^*(\mathbf{r}') v(|\mathbf{r} - \mathbf{r}'|) \varphi_i(\mathbf{r})$  (linear in  $\mathbf{r}$ ), while the central potential is written as  $U(r) = \sum_i \int d\mathbf{r}' |\varphi_i(\mathbf{r}')|^2 v(|\mathbf{r} - \mathbf{r}'|)$ , (independent of  $\mathbf{r}$ ). Of notice that the coupling between e.g. the quadrupole vibration of the core ( ${}^8\text{He}$ ) and a halo neutron is also linear in  $\mathbf{r}$  i.e.  $\langle H_c \rangle_{2^+}(\text{core}, n(\text{halo})) = \beta_2 \left( \frac{R_0}{\sqrt{3}} \frac{du}{dr} \right) O$  (see Sect. 1.9.2).

The many-body effect, at the basis of these phenomena is accomplished in three steps a schematically displayed in Fig. 1.9.1 and 80 described below.

## CHAPTER 1. INTRODUCTION

accurately and economically to propagates renormalization effects which not only renormalizes mean field, but overwhelms it providing a simple explanation of the experimental finding.

Caption Fig. 1.9.1

particle-vibration coupling

${}^9\text{Li}$

① Starting with well defined elements: Woods-Saxon (WS) potential, and the parameters characterizing the low-lying quadrupole vibration of the core (input), calculate the single-particle levels and collective vibration (separable interaction) and determine the corresponding scattering vertices (strength and form factors). From the ratio of the WS radius ( $R_0$ ) and of the observed one ( $R({}^{11}\text{Li})$  input) determine the overlap ①. Because  $\approx 1$ , the contribution of the exchange (Fock) potential to the empirical WS potential is small (energy ( $k$ -) dependent term  $U \approx -50$  MeV +  $U_x$ ,  $U_x = 0.4E(\hbar^2 k^2 / 2m)$ ,  $m_k/m = (1 + ①(m/\hbar^2 k)\partial U_x / \partial k)^{-1}$ ) concerning the halo neutrons, essentially blurring the emergent new Pauli quantum number one (single occupancy) closely related to the many-body Dirac interpretation of the stability of the fully occupied vacuum (Pauli, Dirac, Nobel lectures). Consequently, the neutron halo  $k$ -mass  $m_k$  has a value close to the bare mass  $m$ .

$$V(r_{12}) = -4\pi V_0 \delta(\vec{r}_1 - \vec{r}_2)$$

2 Making use of the above elements one can cloth the bare single-particle states, in particular the  $s_{1/2}$  and  $p_{1/2}$  states. Parity inversion ensues, with  $1/2^+$  and  $1/2^-$  at threshold. As a consequence the  $N = 8$  shell closure melts away,  $N = 6$  becoming a new magic number, testifying to the fact that large amplitude fluctuations are as important or even more important than static mean field effects. As a result  ${}^9\text{Li}_7$  is not bound. Adding one more neutron and switching on the bare pairing interaction (e.g. a contact force  $V$  with constant matrix element  $G = 1.2 \text{ fm}^{-3} V_0/A \approx (28/A) \text{ MeV}$ ) Brink, D. and Broglia (2005), pp 40-42, the screening resulting from the ratio  $r = \frac{(M_j)_{\text{halo}}}{(M_j)_{\text{core}}} \approx \frac{②}{2j+1} \left(\frac{R_0}{R}\right)^3 \approx 0.048$  makes  $(G)_{\text{scr}} = rG$  subcritical, resulting in an unbound system (see Sect. 2.6 and App. 2B).

③ 1

3 Considering the sloshing back and forth of the halo neutron (with a small contribution from the core neutrons) against the core protons, leads to a dipole mode feeling a strongly screened (repulsive) symmetry potential  $\propto (R_0/R)^2 \approx 0.07$  in keeping with the fact,  $\kappa_1 \sim 1/R^2$ . In other words, while the price to pay to separate protons from neutrons in the core is  $5V_1 = 5 \times 33 \text{ MeV} = 165 \text{ MeV}$ , when referring to halo neutrons this price is reduced to  $5 \times 5V_1 = 11.6 \text{ MeV}$  ( $V_1 = 0.07 \times 33 \text{ MeV} = 2.3 \text{ MeV}$ ) for halo neutrons. This fact is at the basis that  $\approx 8\%$  of the Thomas-Reiche-Kuhn sum rule (input) gets down to  $\approx 0.6 \text{ MeV}$ . Another way to say the same thing is that  $(V_1)_{\text{screened}} = ④ V_1$  is at the basis of the fact that the  $E1$  transition  $s_{1/2} \rightarrow p_{1/2}$  ( $\Delta\epsilon \approx 0.3 \text{ MeV}$ ) is only increased by a modest value ( $\hbar\omega_{\text{pygmy}} \approx 0.6 \text{ MeV}; \approx 10^{21} \text{ Hz}$ ), while the  $E1$  single-particle strength remains essentially unchanged (typical values in the case of stable nuclei being  $\approx 10^{-4} B_{sp}(E1)$  for pure low-energy ( $\lesssim 1 \text{ MeV}$ ) single-particle transitions). Now, the two halo neutrons dressed by the vibrations of the core (heavy arrowed lines) and interacting through the bare  $NN$ -pairing force are not bound. Consequently, the pygmy resonance will fade away almost as soon as it is generated (essentially lasting the neutron transversal time

5 upper core

S

a) Brink and Broglia (2005), pp 40-42

the  $s_{1/2} - p_{1/2}$  energy difference

n. 39

version

April 26, 2016

p. 76

that

5

## 1.9. OPTICAL POTENTIAL AND TRANSFER

$\approx 10^{21}$  s, unless. Unless it is exchanged between the two neutron configuration  $s_{1/2}^2(0)$  at threshold ( $2\epsilon_{s_{1/2}} \approx 0.4$  MeV) making it jump into the  $p_{1/2}^2(0)$ , also close to threshold ( $2\epsilon_{p_{1/2}} \approx 1$  MeV). As an intermediate boson, the pygmy resonance which couples to the halo neutron with a strength  $\Lambda \approx 0.62$  MeV (QRPA calculation), contributes to the gluing of the neutron halo Cooper pair with about 1 MeV binding. The corresponding correlation energy  $E_{corr} \approx 0.7$  MeV being mainly due to the pygmy exchange process. The symbiotic halo pair addition mode pygmy GDR of  $^{11}\text{Li}$  can, in principle be used as a building block of the nuclear spectrum, which can be moved around. A possible candidate being the first excited  $0^+$  state of  $^{12}\text{Be}$ , together with the associate dipole state. Because to calculate the giant dipole pygmy resonance (GDR) of  $^{11}\text{Li}$  one needs to know the ground state of this nucleus (halo-pair addition mode) so as to be able to determine microscopically the occupations factor the  $1s_{1/2}, 1p_{3/2}, 1s_{1/2}p_{1/2}, 1s_{1/2}p_{3/2}, \dots$ , etc. states to carry-out a QRPA calculation of the mode. But to do so one needs to know the pygmy. Arrived to this point, one needs to go back to 1 and repeat the whole procedure so as to eventually reach convergence.

### 1.9.4 $^{11}\text{Li}(p, p)^{11}\text{Li}$ optical potential and transfer reaction channels

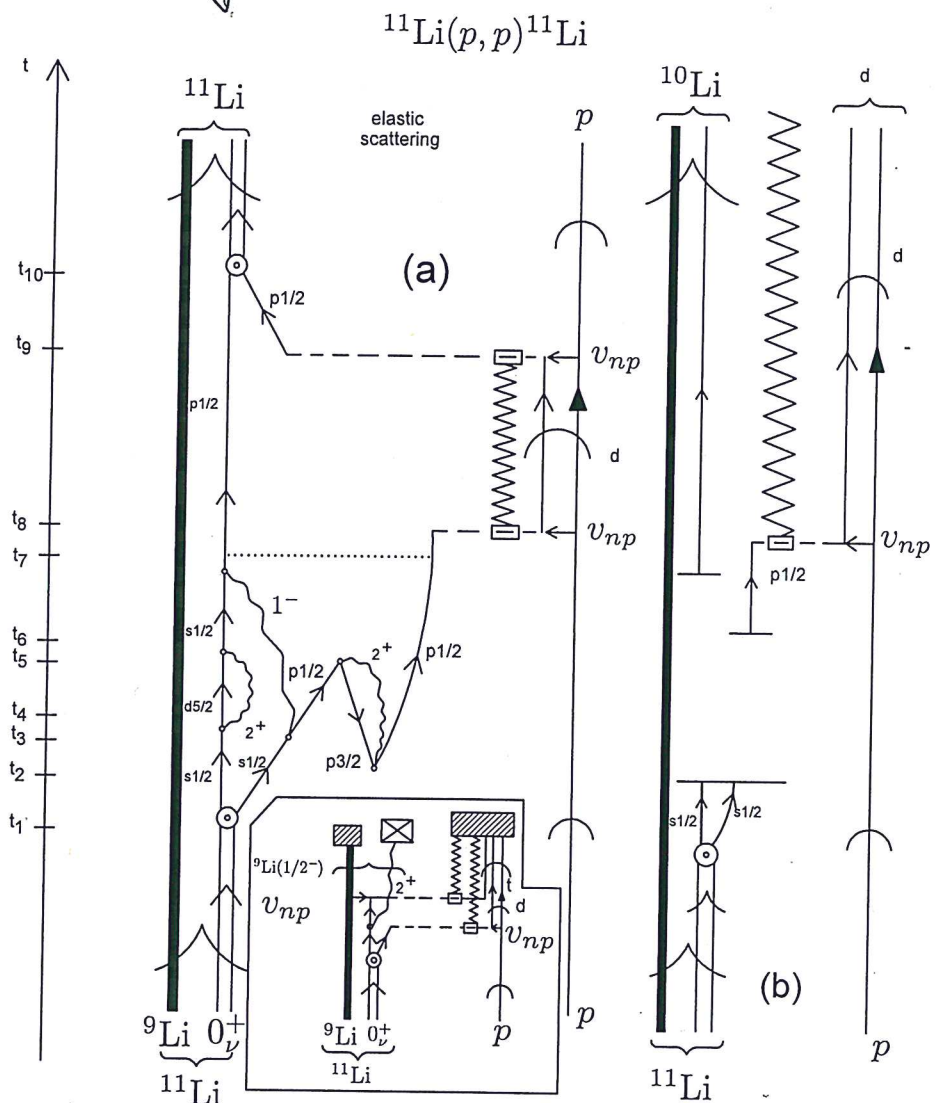
NFT is based on elementary modes of excitation, modes which carry a large fraction of the nuclear correlation. Because its rules have no limitations concerning whether the excitations studied lie or not in the continuum, or whether the single-particle motion displays asymptotic conditions, it allows for a unified description of structure and reactions. An example of the above statement is provided by Fig. 1.9.2. Graph (a) is a NFT-diagram describing one of the processes contributing to the elastic reaction  $^{11}\text{Li}(p, p)^{11}\text{Li}$  as the system propagates in time (polarization contribution to the global (mean field) optical potential describing proton elastic scattering off  $^9\text{Li}$ ). Processes taking place between  $t_1-t_7$ : the halo pair addition mode  $|0_v^+\rangle$  couples at time  $t_1$  with a pure bare configuration and its binding to the  $^9\text{Li}$  core results from parity inversion where the  $s_{1/2}$  continuum orbital is lowered to threshold through coupling with mainly quadrupole vibrational modes and the  $p_{1/2}$  bound state suffers a strong repulsion into a resonant state by Pauli principle with particles participating in the quadrupole mode. The resulting dressed neutron states get bound mainly through the exchange of the  $1^-$  giant dipole pygmy resonance (GDR), represented for simplicity, as a correlated particle-hole excitation, with a small contribution from the bare pairing interaction. At time  $t_8$ , one of the neutrons of the halo Cooper pair is transferred (particle-recoil coupling vertex, see App. 1.D), to the incoming proton projectile through the proton-neutron interaction  $v_{np}$  (prior representation), leading to a deuteron. This neutron is, at time  $t_9$  transferred back (to a virtual  $^{10}\text{Li}$ ) through  $v_{np}$  acting a second time (post representation), with the simultaneous absorption of the recoil mode. Eventually, at time  $t_{10}$  the two neutrons merge, through the particle-pair vibrational coupling, into the halo pair addition mode  $|0_v\rangle$ . The real part of the diagram contributes to  $U_{opt}$  while the imaginary one to  $W_{opt}$ , corresponding to the real and imaginary (absorptive)

(screening effect, see previous subsection)

vertex

insert last Fig.  
Andrea used in Plays.  
scripta

## CHAPTER 1. INTRODUCTION



- $\uparrow$  neutron pair halo
- $\circ$  particle-vibration coupling vertex
- $\odot$  particle-pair vibration coupling vertex
- $v_{np}$  proton-neutron int.
- $\swarrow$  recoil mode
- $\uparrow$  neutron
- $\uparrow$  proton } bound
- $^{2+} \not\lesssim ^9\text{Li}$  core quadr. vibr. mode
- $^1 \not\lesssim ^{11}\text{Li}$  giant dipole pygmy resonance mode
- $\square$  particle-recoil mode coupling vertex
- $\oplus$  deuteron continuum
- $\dagger$  proton continuum
- ... monopole interaction

✓ Figure 1.9.2: NFT diagram describing (a) one of the processes contributing to the elastic reaction  $^{11}\text{Li}(p,p)^{11}\text{Li}$  and (b) to the  $^{11}\text{Li}(p,d)^{10}\text{Li}$  process.

1.9. OPTICAL POTENTIAL AND TRANSFER

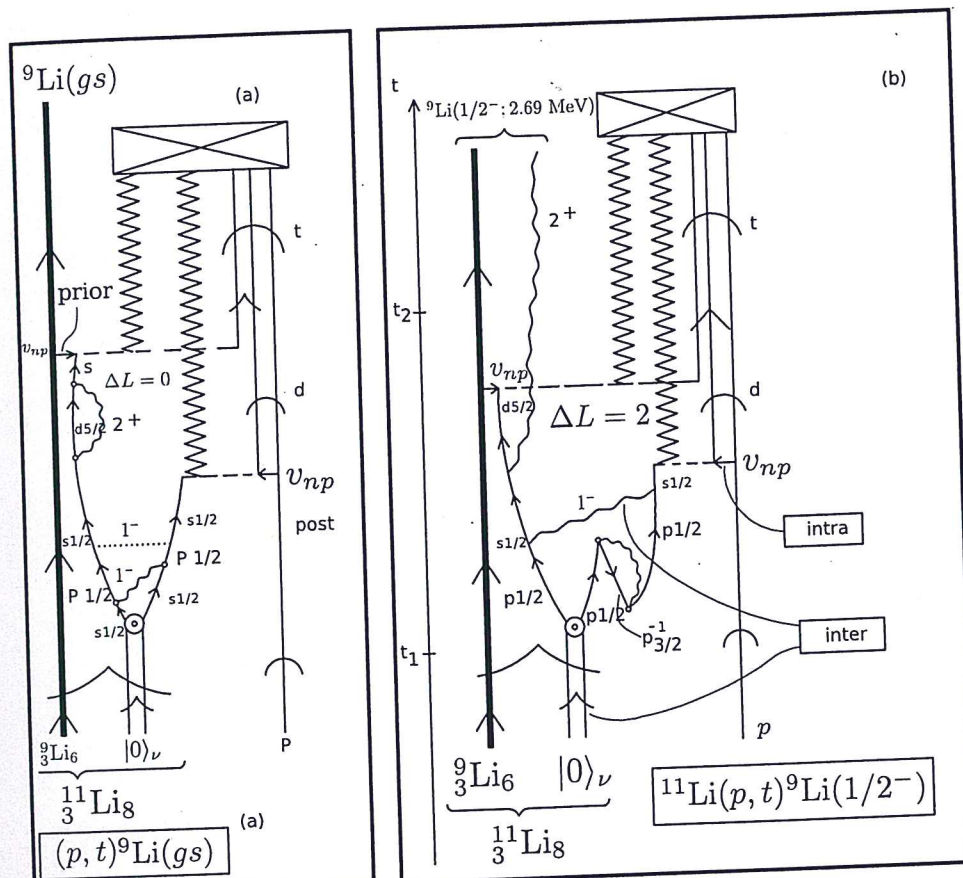
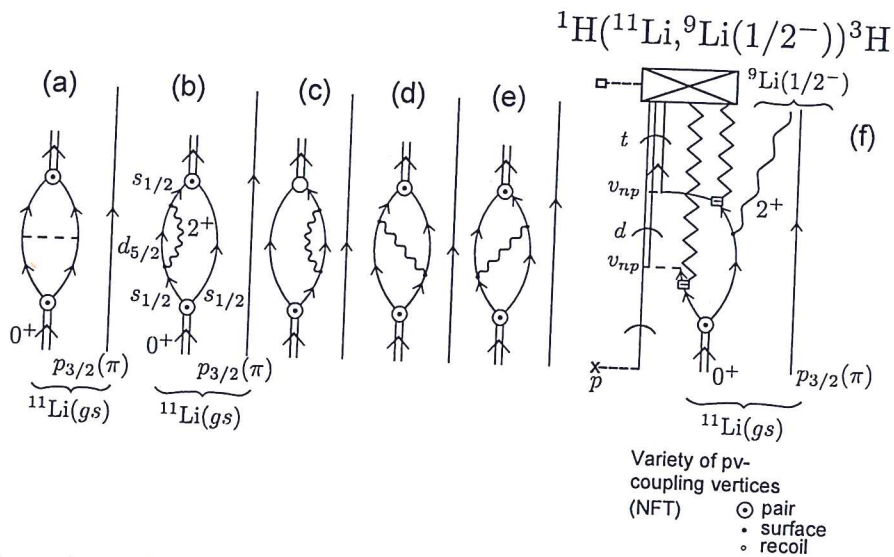


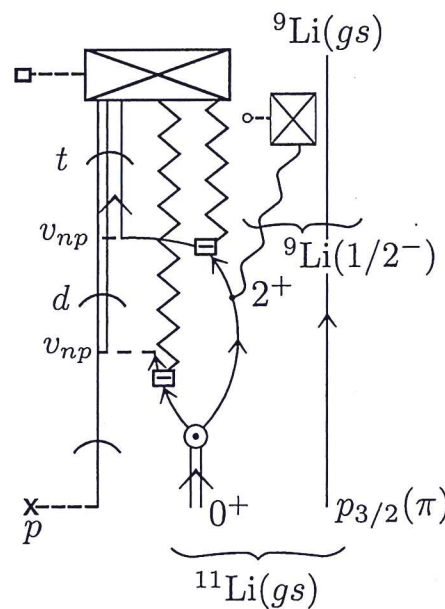
Figure 1.9.3: NFT-graphical representation of contributions to (a)  $^{11}\text{Li}(p, t)^9\text{Li}(\text{gs})$  and (b)  $^{11}\text{Li}(p, t)^9\text{Li}(1/2^-)$  reactions. The dotted horizontal line in (a) represents the  $NN$ -symmetry potential. The boxed labels in (b) indicate the bare ( $v_{np}$ ) and phonon mediated interactions which bind the Cooper pair to the core  $^9\text{Li}$  (intra), and those acting between target and projectile (eventually) also outgoing particle (inter). For more details see text. Time is assumed to run upwards. A single arrowed line represents a fermion (proton) ( $p$ ) or neutron ( $n$ ). A double arrowed line two correlated nucleons. In the present case two correlated (halo) neutrons (halo-neutron pair addition mode  $|0\rangle_\nu$ ). A heavy arrowed line represents the core system  $^9\text{Li}(\text{gs})$ . A standard pointed arrow refers to structure, while "round" arrows refer to reaction, regardless whether they are in the continuum or less. A wavy line represents (particle-hole) collective vibrations, like the low-lying quadrupole mode of  $^9\text{Li}$ , or the more involved dipole pigmy resonant state which, together with the bare pairing interaction (horizontal dotted line) binds the neutron halo Cooper pair to the core. A short horizontal arrow labels the proton-neutron interaction  $v_{np}$  responsible for the single-particle transfer processes, represented by an horizontal dashed line. The jaggy curve represents the (collective) recoil effect resulting from the mismatch between the relative centre of mass coordinates associated with the mass partitions  $^{11}\text{Li}+p$ ,  $^{10}\text{Li}+d$  (virtual), and  $^9\text{Li}+t$ .



✓ Figure 1.9.4: Lowest order, NFT diagrams associated with the processes contributing to the binding of the neutron halo Cooper pair (double arrowed line) of  $^{11}\text{Li}$  to the core  $^9\text{Li}$  through the exchange of the core quadrupole phonon (wavy line). Single arrowed lines describe the nucleon independent-particle motion of neutrons ( $s_{1/2}$ ,  $d_{5/2}$ , etc.) as well as of protons ( $p_{3/2}(\pi)$ ). (a) Bare interaction, four-point vertex (horizontal dashed line); (b, c) self energy, effective mass process dressing the  $s_{1/2}(\nu)$  single-particle state; (d, e) vertex correction (induced interaction) renormalizing the pair addition mode coupling vertex with which it couples to the fermion (dotted open circle); (f) NFT diagrams describing the reaction  $^1\text{H}(^{11}\text{Li}, ^9\text{Li}(1/2^-; 2.69 \text{ MeV})) ^3\text{H}$  populating the first excited state of  $^9\text{Li}$ . The jagged line represents the recoil mode carrying asymptotically to the detector the effect of the momentum mismatch associated with the transfer process (recoil). In this case of successive transfer, one for each transferred neutron ( $^{11}\text{Li}(\text{gs}) + p \rightarrow ^{10}\text{Li} + d \rightarrow ^9\text{Li}(1/2^+) + t$ ). For details see Sect. (2.6) as well as Sect. (6.1).

the pair addition mode

inverse kinematics



Variety of pv-coupling vertices

(NFT)       $\odot$  pair  
               • surface  
                $\square$  recoil

✓ Figure 1.9.5: Gedanken  $\gamma$ -ray coincidence experiment  ${}^1\text{H}({}^{11}\text{Li}, {}^9\text{Li}){}^3\text{H}$  and  ${}^9\text{Li}(gs) + \gamma$  ( $E2; 2.69 \text{ MeV}$ ). In this case, the virtual quadrupole phonon associated with self-energy and vertex correction processes becomes real through the action of the  $(p, t)$  external field. Thus, it is not only the recoil modes "measured" by particle detectors which have asymptotic wavefunction, but also the quadrupole vibration, which is measured by the  $\gamma$ -detector. For details see Caption Fig. 1.9.4.

in connection with outgoing particles

whose eventual  $\delta$ -decay can be

"measured"

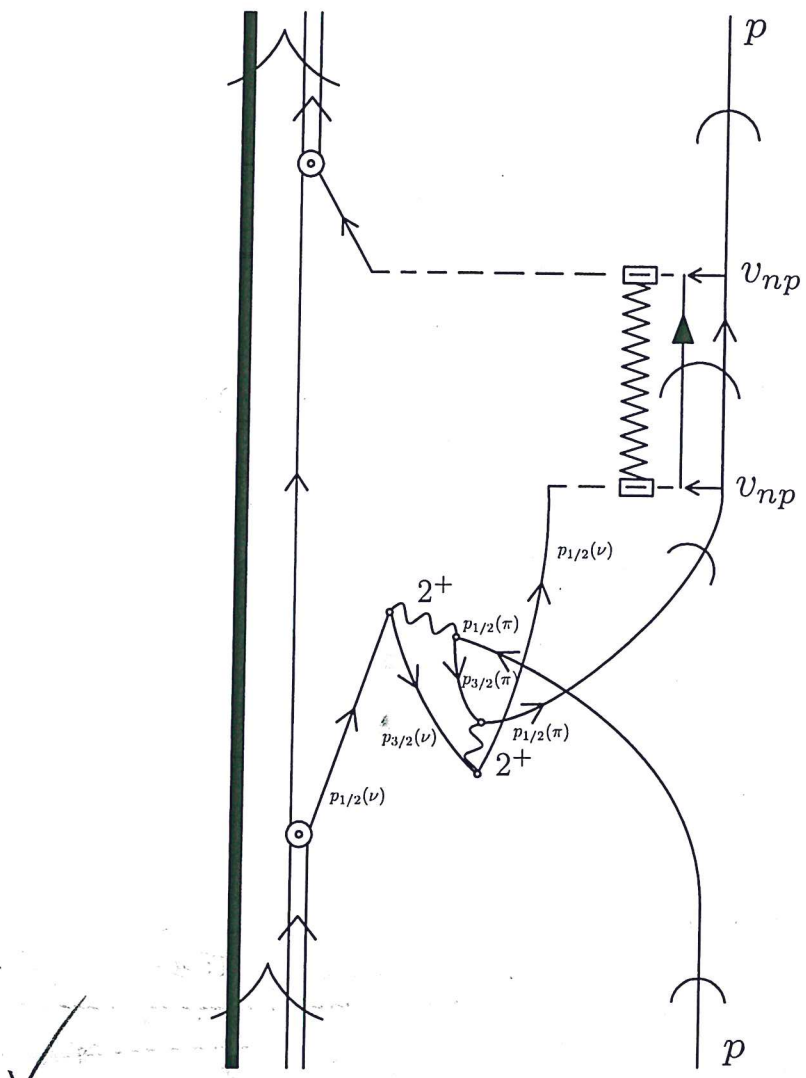


Figure 1.9.6: In keeping with standard direct reaction praxis, neither in Fig. 1.9.2 nor in 1.9.3 antisymmetrization is carried out between the impinging proton and the protons of  $^{11}\text{Li}$ . Within the present discussion ( $^{11}\text{Li}(p, p)^{11}\text{Li}$ ) (see Fig. 1.9.3), an example of such processes corresponds to the exchange of a proton participation in the quadrupole vibration of the core, with the projectile, as shown in the figure. Such a process will not only be two orders higher in perturbation in the particle-vibration coupling vertex. It will be strongly reduced by the square of the overlap between a proton moving in the continuum, and a  $p_{1/2}$  proton of the  $^9\text{Li}$  core bound by about 10 MeV.

participating

### 1.10. SUMMARY

component of the polarization contribution to the optical potential, to be added to the experimental determined (global)  ${}^9\text{Li} + p$  elastic scattering optical potential. It is of notice that this diagram exemplifies the elements needed to extend and formalize NFT rules of structure so as to be able to deal also with reactions. In Fig. 1.9.2 (b) one assumes the same processes to take place as in (a) up to time  $t_8$  (reason for which no details are repeated between  $t_2$  and  $t_8$ ). From there on the deuteron continues to propagate to the detector, and the effect of the particle-recoil coupling vertex is to be worked out and the corresponding outgoing distorted waves modified accordingly. Likely, the neutron in  ${}^{10}\text{Li}$  will break up before it can be recorded by the particle detector. Summing up, in the center of mass reference frame both  $p$  and  ${}^{11}\text{Li}$  display asymptotic states in entrance as well as in exit channels in case (a), and only in the entrance channel in case (b), while in the exit channel only  ${}^{10}\text{Li}({}^9\text{Li}+n)$  and the deuteron do so. *(likely for)*

Another examples of the NFT diagrams of structure and reactions are given in Fig. 1.9.3. In (a) one contribution associated with the reaction  ${}^{11}\text{Li}(p, t){}^9\text{Li}(\text{gs})$  is shown, while in (b) one associated with the population of the first excited  $1/2^-$  (2.69 MeV) state of  ${}^9\text{Li}$ . Within this context we refer to Figs. 1.9.4 and 1.9.5 for a compact graphical representation of this last process. The importance of this process is that it provided, for the first time, direct evidence of phonon mediated pairing interaction in nuclei as theoretically predicted<sup>74</sup>.

Returning to the process displayed in Fig. 1.9.2 concerning the question of Pauli principle (also essential in the case of structure NFT), in this case not between e.g. the two halo neutrons, but between the incoming proton and the collective modes of the core ( ${}^9\text{Li}$ ) we refer to Fig. 1.9.6. It is of notice that making use of global optical potentials to describe the elastic channel, or mean field optical potentials to which to add polarization contribution like those displayed in Fig. 1.9.2 (a), the effect of Pauli principle between a nucleon projectile and the nucleons of the target is considered through the energy ( $k$ -dependent strength, so-called Perey-Buck potential<sup>75</sup>) (intimately connected with the  $k$ -mass) (see Eq. (1.9.2)).

*(can, approximately, be taken care of through the energy - ( $k$ -) dependent  $k$ -mass)*

### 1.10 Summary and Table 1.4.1

In Fig. 1.10.1<sup>76</sup> the results of a "complete" NFT(r+s) description of the open shell superfluid nucleus  ${}^{120}\text{Sn}$  in terms of the  ${}^{120}\text{Sn}(p, t){}^{118}\text{Sn}(\text{gs})$ ,  ${}^{122}\text{Sn}(p, t){}^{120}\text{Sn}(\text{gs})$ ,  ${}^{120}\text{Sn}(p, d){}^{119}\text{Sn}$ ,  ${}^{121}\text{Sn}(p, d){}^{120}\text{Sn}$ ,  ${}^{119}\text{Sn}(\alpha, \alpha'){}^{119}\text{Sn}$  ( $\gamma$ -decay) cross sections, energies and transition probabilities are displayed in comparison with the experimental findings. Arbitrarily forcing the (PVC) strength, the strength of the bare pairing force and the value of the  $k$ -mass to depart from their "physical" values, one can test the robustness of the NFT(r+s) picture of  ${}^{120}\text{Sn}$  given, and of the well funneled character of the associated nuclear structure and reaction landscape<sup>77</sup> (Idini et al.

<sup>74</sup>Barranco, F. et al. (2001) Tanihata, I. et al. (2008); Potel et al. (2010); Tanihata et al. (2013); Beccio-Novò et al. (2015).

<sup>75</sup>Perey and Buck (1962).

<sup>76</sup>Footnote see pg

<sup>77</sup>Idini et al (2015)

F - F

PPD  
April 2011

(F\*) In relation with the program of NFT(r+s) one can mention that Landau felt that <sup>87a</sup> Feynman diagrams have an independent basic importance, because the possibility of relating them directly to physical observables. Feynman diagrams allow to describe processes where one set of particles, with given energies, momenta, angular momenta, go in and another set (or the same) comes out. At the basis of this approach one finds vertex processes and dispersion relations. Now, vertex processes can simply mean the variety of processes connecting the incoming particle, with the outgoing ones. In other words, within the present framework the processes taken place between times  $t_2 - t_{10}$  (Fig. 1.9.2) and  $t_1 - t_2$  (Fig. 1.9.3) (Landau (1959), see also ter Haar (1969)).

(F)

top. 80 ch. I

---

ter Haar, D. Men of Physics: L. D. Landau II, Pergamon Press, Oxford (1969).

Landau, L. D. On analytic properties of vertex parts in quantum field theory, Nucl. Phys. 13, 181 (1959).